A Note on Leakage Jet Forces: Application in the Modelling of Digital Twins of Hydraulic Valves

Zoufiné Lauer-Baré[1,*], Erich Gaertig[1], Johannes Krebs[1], Christian Arndt[1], Christian Sleziona[1] and André Gensel[2]

[1]*Simulation Department, Hilite Germany GmbH, Nürtingen, Germany*
[2]*Testing Department, Hilite Germany GmbH, Nürtingen, Germany*
E-mail: zoufine.lauer-bare@hilite.com
[*]Corresponding Author

Abstract

The proper modelling of fluid flow through annular gaps is of great interest in leakage calculations for many applications in fluid power technology. However, while detailed numerical simulations are certainly possible, they are very time consuming, in various cases prone to numerical instabilities and may not even include all physically relevant effects. This is an issue especially in system simulations, where a large set of computations is needed in order to prepare the lookup-tables for the required input fields. In this work, an analytical approximation for the shear force, which is induced by viscous flow between two eccentric cylinders, is presented. This relation, and its derivation, mimics and enhances the well-known Piercy-relation for the corresponding volume flow that is utilized in state-of-the-art system simulation tools. To determine its range of validity, the analytical relation for the shear force is compared to 3D-simulations. Additionally, an application of this approximation for creating digital twins of hydraulic valves is also discussed in this work.

1 Introduction

The flow through annular gaps is of great interest in all areas of fluid power technology, see for instance [10, 5, 16], where the flow is caused by internal leakage of valves. Other applications of this kind can be found in petroleum engineering; see e.g. [6, 9], or in the nuclear sciences (see [1]) in the context of two-phase flows. It is also utilized for hemodynamic studies in medical appliances; see for instance [24] for a study of the blood flow in arteries. In general, the fluid flow through an annular domain between two cylinders is viscous and induces shear forces (leakage jet forces, viscous flow forces) that act upon the surface of the inner cylinder; see [21] or [4]. These forces can either be computed numerically, which requires detailed meshing and is time consuming, or in certain simple cases analytically, which then yield results that are as accurate as equivalent numerical findings from full 3D-simulations.

For further reference and as the general setup for the following discussion, Figure 1 shows two concentric cylinders of length l, inner radius R_1 and outer radius R_2, oriented along the positive z-axis. The annular flow domain mentioned above is contained in the region between these two cylinders.
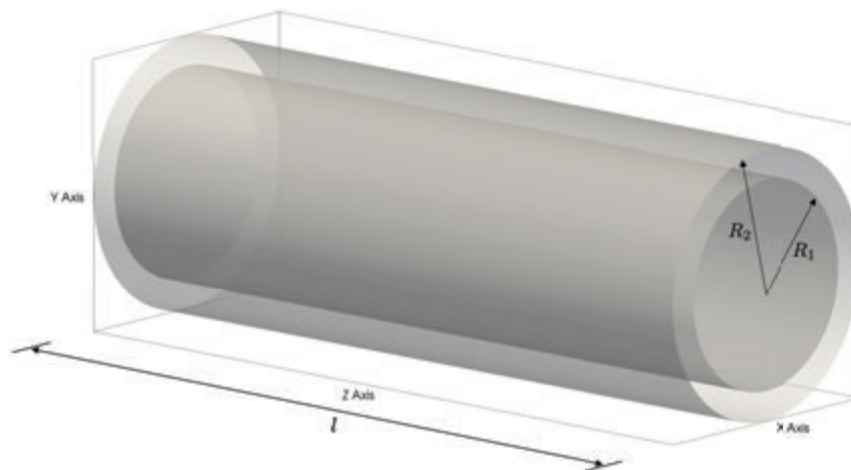
Figure 1   General setup of fluid flow in a cylindrical gap.
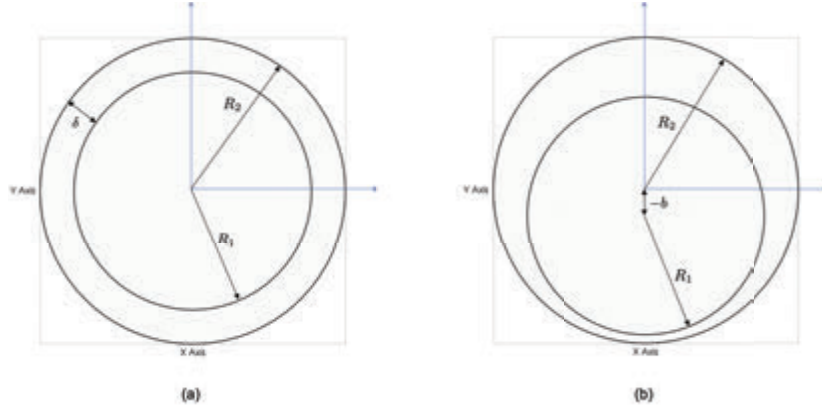
Figure 2 Cross sections of the cylinders of Figure 1, concentric case (a) and eccentric case (b).

The following Figure 2 shows the corresponding cylinder cross sections in the xy-plane both without and with eccentricity. The latter case is included here since it is conceptually the most challenging and interesting one; it is also very common in practice as perfect concentricity is rarely obtained in realistic applications.

In the eccentric case, Figure 2(b), the inner cylinder is displaced vertically from the common symmetry axis by a value of $-b$, where $b > 0$ is called the absolute eccentricity. On the other hand, the relative eccentricity ε is defined by $\varepsilon = b/\delta$, where $\delta = R_2 - R_1$ is the difference between outer and inner radius (see Figure 2(a)).

In this work we will establish a connection between the shear force F_e, that is induced by the viscous flow in between two eccentric cylinders, and its corresponding concentric counterpart F_c by a relation of the form

$$F_e \approx F_c(1 + a(\kappa)\,\varepsilon^2), \tag{1}$$

where $a(\kappa)$ is a scale-invariant correction term that only depends on the intrinsic geometry of the system, i.e. the ratio of inner to outer radius, $\kappa = R_1/R_2$. In particular, F_c is the leading term in a 2nd-order Taylor-expansion of F_e around $\varepsilon = 0$. As far as we can tell, this relation was unknown previously.

Simplifying even further, since the correction term $a(\kappa)$ is a rather complicated expression in κ, using its derivative to obtain a linear approximation around $\kappa = 1$ leads to a very convenient recipe for jet forces in many

applications where $R_1 \approx R_2$, i.e.

$$F_e \approx F_c \left(1 + \frac{(\kappa - 1)}{6} \, \varepsilon^2 \right) \quad \text{for } \kappa \approx 1. \tag{2}$$

Following this derivation, we will demonstrate an application of relation (1) in the context of assembling look-up tables for jet forces, which can be used to create a digital twin of hydraulic valves. The concept of a digital twin in this article consists of a complex system-simulation model which includes data from all relevant sub-systems (e.g. fluid forces, magnetic forces, stresses, …). This component is then utilized as a digital twin of hydraulic valves in an automotive system modelling software like Simcenter Amesim.

When implementing the currently available analytical relations for F_e and F_c, due to singular terms the expression for F_e the eccentric case does not reduce easily to the concentric one for $\varepsilon = 0$. It has to be evaluated either by a limiting process or one would need to switch between F_e and F_c depending on the actual geometry. A similar and well-known situation occurs for the corresponding flow rates Q_e and Q_c. However, in this case a relation like Equation (2) is known in the form of (see [21])

$$Q_e \approx Q_c(1 + 1.5 \, \varepsilon^2). \tag{3}$$

This approximation is very popular (see for instance [10] or [26]) and is used as state-of-the-art leakage flow model in modern system simulation tools. The proposed Equation (1) is a universal relation for the shear forces and either this expression or its more manageable limit (2) could be implemented as part of the Simcenter Amesim component "BRF01".

This article is structured as follows: In the following Section 2 the utilization of relation (1) is motivated within the context of generating input data for a digital twin (as defined above). Furthermore, it is reviewed how the current analytical approximations for F_e, F_c, Q_e and Q_c can be derived from the incompressible, steady-state Navier-Stokes equations and why the currently available relation for F_e does not easily reduce to F_c.

In Section 3 the motivation for the approach chosen here is briefly demonstrated for an already known case. Afterwards, the main result of this work, relation (1) along with the expression for the coefficient $a(\kappa)$, is derived by a Taylor-expansion around $\varepsilon = 0$. In addition the domain of validity of (1) is discussed, also with regard to approximation (2).

In Section 4 the general setup for the corresponding 3D-simulations of leakage jet forces with Ansys CFX is described. The analytical relation for

the jet force F_e is then compared to its proposed approximation as well as to the numerical value obtained in a post-processing step from CFX. This will show the high accuracy of the analytical approximation if the necessary conditions for its application are met.

Finally, in Section 5 the flow rate-curves of the digital twin described in Section 2 are compared to testing results. The good agreement between system simulation and actual measurements motivates the inclusion of 3D-effects into digital twins for hydraulic components. They can be used for the development of hydraulic products that incorporate these components as sub-models.

## 2 Hydraulic Valves and Digital Twin Technology

The motivation for deriving relation (1) originates from the necessity to create digital twins for magneto-hydraulic proportional valves as shown in the following Figure 3. The interplay between magnetic and hydraulic forces is harnessed here in order to control the flow of oil to and from the various ports labelled T, B, P and A in the figure below.

There are several different ways, the notion of a digital twin is used in current literature. An approach similar to the one presented here describes a digital twin as a component in a system simulation environment; see e.g. [14]. However, simulation based digital twins may also interact with their hardware surroundings as described in [27]. Additionally they can even continuously evaluate testing data obtained from appropriate sensors; see for instance [12].

In our case the digital twin is a virtual Amesim representation of the valve depicted in Figure 3 (an Amesim component). The necessary input fields
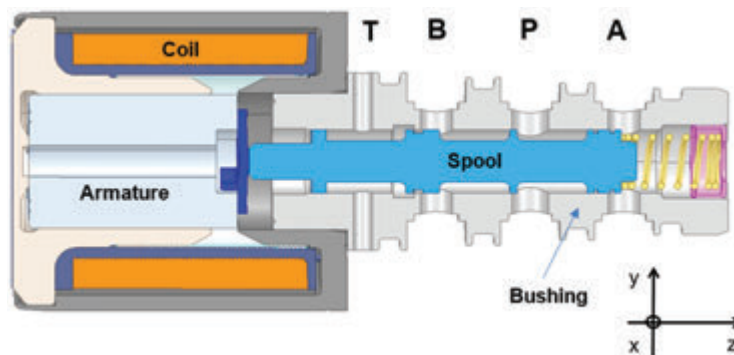
Figure 3   Cross section of a typical magneto-hydraulic proportional valve.
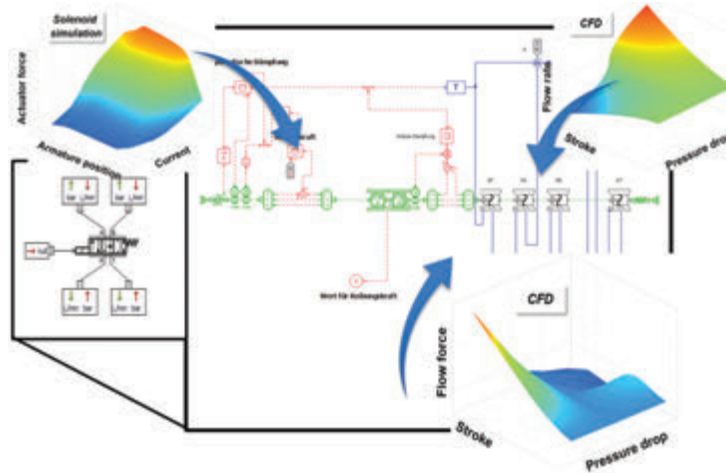
Figure 4 Linking input fields as lookup-tables into a complex, multi-domain system simulation model.

of the magnetic force are computed by axisymmetric 2D-FEM-simulations while the results for the flow forces are based on 3D-FVM-models. The generated data can be incorporated as a parametrized righthand-side for the equation of motion in a system simulation tool such as Amesim. In particular, the relevant CFD-fields which depend on pressure drop, stroke position and fluid temperature can be included in the digital twin by utilizing Amesim's Signal and Control library. When using this component in a system simulation model of the test rig, the digital twin picks the temperature from the oil property component (labelled "FP04" in the Amesim library) and the corresponding CFD data is used. This general idea is sketched in the following Figure 4.

The details of the method described here are not relevant for the main goal of this article; the interested reader is referred to [8] for the magnetic field simulations and to [7, 11] for additional information on the CFD-methods and system simulation. Concerning the flow rate- and jet force-modelling, numerical, analytical and hybrid techniques are available; see for instance [3, 2, 15]. In particular, a contribution modelling flow rates in valves analytically with an orifice equation approach was presented in [23]. There is vibrant activity both in the industrial and academic sector concerning these topics, hence this reference list is not exhaustive at all.

The flow rate and the force that act on the spool of a magneto-hydraulic valve can be computed in a postprocessing step once the velocity distribution

$\mathbf{v} = (v_x, v_y, v_z)^T$ is obtained as solution to the incompressible, steady-state Navier-Stokes equation (gravity is neglected here)

$$\rho \left(\mathbf{v} \cdot \nabla\right) \mathbf{v} - \mu \, \Delta \mathbf{v} + \nabla p \,=\, 0 \tag{4}$$

$$\nabla \cdot \mathbf{v} \,=\, 0. \tag{5}$$

Equation (4) is the momentum equation for a fluid with density ρ, dynamic viscosity μ and pressure p; the subsequent Equation (5) ensures conservation of mass in the time-independent and constant-density case considered here.

The PDEs of (4), (5) need to be supplied by proper boundary conditions; in our case these are given by

$$\mathbf{v} \,=\, 0 \qquad \text{on inner and outer walls}$$
$$p \,=\, p_0 \qquad \text{at inlet}$$
$$p \,=\, p_l \qquad \text{at outlet}$$

However, when compiling the necessary jet force-fields for the digital twin, the question emerges which values for the forces should be included especially in the overlap area of the stroke. A detailed numerical leakage-simulation of system (4)–(5) for this type of geometry is very time consuming and just setting the fluid force to zero there by brute-force will neglect physical effects and may lead to numerical instabilities; see [18] or [17]. This artificial commitment to vanishing jet-forces when feasible is depicted in Figure 5; numerically computed values are available in a range between 0 mm and 0.1 mm.

The jet forces shown in this figure are negative because the BT fluid flow is directed towards the negative z-direction in the coordinate system of Figure 3 and laminar flows induced by a pressure drop lead to jet forces in direction of the flow (see [4] and the following Equations (7)–(9)).

The search for an effective and accurate way of dealing with the regions indicated by question marks in Figure 5 is the main motivation in this article for taking a closer look at analytic relations for the shear force induced by an annular flow between two cylinders.

When the path BT is about to close, the relevant flow domain can be modelled as an annular gap as depicted schematically in Figure 1 and Figure 2. This domain is also depicted in the following Figure 6 for the actual valve used here.

Since in this case the flow is dominated by the axial component, the original Navier-Stokes equation reduces to the linear Stokes problem, i.e.
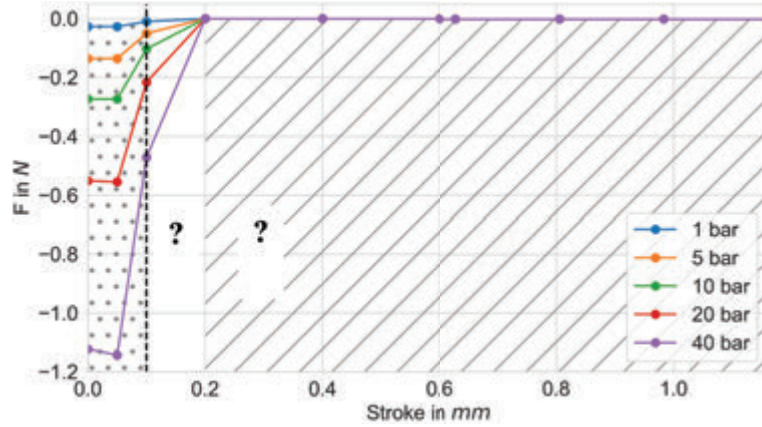
Figure 5   Jet force acting on the spool when the path BT is closed by the spool in Figure 3.
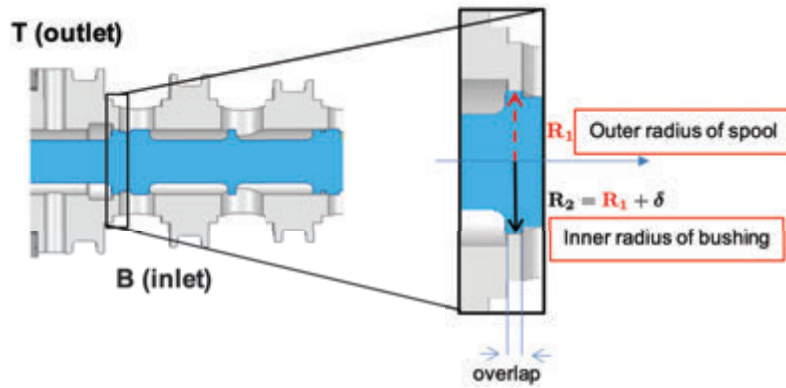

Figure 6   Cross-section view of bushing and spool and zoomed metering edge, where the spool is in a stroke position that closes BT.

an ordinary differential equation; see [21] for example. Using cylindrical coordinates and the divergence constraint (5), the PDE-system (4) can be recast into

$$-\mu \left(\frac{1}{r} \frac{\mathrm{d}}{\mathrm{d}r} + \frac{\mathrm{d}^2}{\mathrm{d}r^2} \right) u = \frac{\Delta p}{l}, \quad R_1 < r < R_2 \tag{6}$$

with boundary conditions

$$u(R_2) = 0$$
$$u(R_1) = 0.$$

Here, $u = v_z$ denotes the axial component of the velocity vector $\mathbf{v}$ and $\Delta p = p_0 - p_l$ indicates the pressure drop. The advantage of this type of equation is that for certain flow domains it can be solved analytically. After obtaining the velocity distribution, it is a simple post-processing step to compute the corresponding jet force. The solutions of (6) depend only on the distance to the symmetry axis of the outer cylinder (with Radius R_2) and integrating them leads straight to flow rates and shear forces. Hence, in cases where the flow is almost purely axial, the Stokes equation already contains the full information of the original system (4)–(5); no time-consuming CFD needed. It is also worth mentioning, that in these cases there is no need for any additional calibration or fitting of the flow rate or flow force as in the case of an analytical orifice equation approach. There, an auxiliary parameter, the so-called discharge or contraction coefficient, is introduced which is not uniquely determined by the Navier-Stokes equations. This coefficient re-implements viscosity-driven effects that are neglected in the Euler- and Bernoulli-equations and are therefore also missing in the resulting orifice equation (see [25] or [13]).

When the relevant shear stresses are integrated over the surface of the inner cylinder, one obtains two different flow force relations, depending on eccentricity. For instance from [4] it is known that in the concentric case, $\varepsilon = 0$, the jet force acting on the inner cylinder is given by

$$F_c = -\pi \Delta p \left(R_1{}^2 - \frac{\left(R_2{}^2 - R_1{}^2 \right)}{2 \ln \left(R_2/R_1 \right)} \right). \tag{7}$$

As described above, this relation is obtained by integrating the corresponding shear stress over the surface of the inner cylinder, i.e.

$$F_c = \int_0^l \int_0^{2\pi} \left(\mu \, r \frac{\mathrm{d}}{\mathrm{d}r} u(r) \right)_{r=R_1} \mathrm{d}\varphi \, \mathrm{d}z, \tag{8}$$

where the axial velocity component ist given by

$$u(r) = \frac{\Delta p}{4\mu l} \left(R_2{}^2 - r^2 - \left(R_2{}^2 - R_1{}^2 \right) \frac{\ln \left(R_2/r \right)}{\ln \left(R_2/R_1 \right)} \right). \tag{9}$$

Analogously, for the "strict" eccentric case $0 < \varepsilon < 1$ it is known from e.g. [21] that again by integrating the shear stress, the force acting on the surface of the inner cylinder is given by

$$F_e = -\pi \Delta p \left(R_1{}^2 - \frac{bA}{\beta - \alpha} \right), \tag{10}$$

where

$$A = \sqrt{B^2 - {R_2}^2}, \ B = \frac{1}{2b}\left({R_2}^2 - {R_1}^2 + b^2\right) \tag{11}$$

and

$$\alpha = \frac{1}{2}\ln\left(\frac{B+A}{B-A}\right), \ \beta = \frac{1}{2}\ln\left(\frac{B-b+A}{B-b-A}\right). \tag{12}$$

An implementable formulation of the corresponding velocity distribution can be found for instance in [22].

Unfortunately as one can see from Equation (10), it is not immediately clear what happens in the concentric case, i.e. for $\varepsilon = b = 0$. Simply evaluating this expression for $b = 0$ is not allowed since one would divide by 0. Of course one could compute F_e in a limiting process for ever decreasing values of b but this procedure does not at all shed a light on how exactly Equation (10) reduces to Equation (7) in the concentric case.

In the following Section 3 we will therefore derive a practical relation that unites the jet forces for all relative eccentricities, e.g. Equation (1).

3 Analytical Modelling of Leakage Jet Forces

As motivation for our approach, let us start again by considering the different flow rates obtained by solving the Stokes problem for the geometries shown in Figure 2. As already mentioned in the introduction, the flow rate for the eccentric case, Q_e, is related to its concentric counterpart Q_c by the approximate relation (3), where (see e.g. [21, 26])

$$Q_c = \frac{\pi\Delta p}{8\mu l}\left({R_2}^4 - {R_1}^4 - \frac{\left({R_2}^2 - {R_1}^2\right)^2}{\ln\left(R_2/R_1\right)}\right). \tag{13}$$

Similar to the flow force computation leading to (7), (13) is obtained in a post-processing step by integrating the very same velocity distribution (9), which solves the Stokes Equation (6) within a concentric annulus,

$$Q_c = \int_{R_1}^{R_2}\int_0^{2\pi} r u(r)\mathrm{d}\varphi\,\mathrm{d}r. \tag{14}$$

There is also an expression for the corresponding flow rate in the eccentric case, albeit as an infinite series representation (see [21]), given by

$$Q_e = \frac{\pi\Delta p}{8\mu l}\left({R_2}^4 - {R_1}^4 - \frac{4b^2 A^2}{\beta - \alpha} - 8b^2 A^2 \sum_{k=1}^{\infty}\frac{k\mathrm{e}^{-k(\beta+\alpha)}}{\sinh\left(k(\beta-\alpha)\right)}\right). \tag{15}$$

Relation (3) seems to be a truncated Taylor-expansion of Equation (15) in the relative eccentricity around $\varepsilon = 0$, although to the best of our knowledge, the expansion itself is never made explicit in current literature. Now an obvious question related to this discussion is, whether there exists an approximation, relating the jet force F_e of the eccentric case to its concentric counterpart F_c in a similar manner as relation (3) does for the flow rates.

In order to illustrate this point further, let us recall that this approach is already very common in oil hydraulics. The popular approximation (see [10]) for the flow rate in the concentric case

$$Q_1 = \frac{\pi \Delta p\, R_1}{6\mu l}\, \delta^3, \tag{16}$$

which is also used in the Simcenter Amesim 16.1 component "BAF01" and in DSHPlus (see [20]), is simply the leading term in a Taylor-expansion of Equation (13) around $\delta = 0$ (R_1 is kept fixed there and R_2 is replaced by $R_1 + \delta$). In [26] one can even find the next term (of fourth order) in this expansion, which is not widely used in fluid power literature though, i.e.

$$Q_2 = \frac{\pi \Delta p\, R_1}{6\mu l}\left(\delta^3 + \frac{1}{2R_1}\delta^4\right). \tag{17}$$

As a sidenote, it is also rather straightforward to calculate higher-order corrections for this truncated Taylor-series. For example including the fifth order term (not seen by the authors in the literature by now), the corresponding expansion now reads as

$$Q_3 = \frac{\pi \Delta p\, R_1}{6\mu l}\left(\delta^3 + \frac{1}{2R_1}\delta^4 + \frac{1}{60R_1{}^2}\delta^5\right). \tag{18}$$

Following this idea, Equation (10) for the jet force is regarded as a function of the relative eccentricity ε and a Taylor-expansion around $\varepsilon = 0$ is carried out. Assuming analyticity of F_e (that is, the Taylor-expansion of (10) is identical to F_e within its convergence radius), we can write

$$F_e(\varepsilon) = F_e(0) + \left.\frac{\mathrm{d}F_e(\varepsilon)}{\mathrm{d}\varepsilon}\right|_{\varepsilon=0}\varepsilon + \frac{1}{2}\left.\frac{\mathrm{d}^2 F_e(\varepsilon)}{\mathrm{d}\varepsilon^2}\right|_{\varepsilon=0}\varepsilon^2 + \mathcal{O}(\varepsilon^3) \tag{19}$$

and truncate the expression after the quadratic term. For practical calculations it is actually more convenient to work with the absolute eccentricity b as dependent variable since (10) is already expressed in that way. After evaluating the required derivatives, it is an easy application of the ordinary chain

rule to switch to ε as expansion parameter, i.e. $\mathrm{d}F/\mathrm{d}\varepsilon = \mathrm{d}F/\mathrm{d}b \cdot \mathrm{d}b/\mathrm{d}\varepsilon = (R_2 - R_1)\mathrm{d}F/\mathrm{d}b$.

As a simple example for this approach, let us derive the constant term in (19) which is identical to $F_e(b = 0)$ in (10) and does not include any derivatives at all. The only non-trivial part there is the second term in parentheses; we will consider numerator and denominator separately.

From the Definitions (11), (12) it is clear that

$$bA = b\sqrt{B^2 - R_2{}^2} = b\sqrt{\frac{1}{4b^2}\left(R_2{}^2 - R_1{}^2 + b^2\right)^2 - R_2{}^2}$$
$$= \sqrt{\frac{1}{4}\left(R_2{}^2 - R_1{}^2 + b^2\right)^2 - b^2 R_2{}^2}$$

and therefore

$$\lim_{b\to 0}(bA) = \frac{1}{2}\left(R_2{}^2 - R_1{}^2\right). \tag{20}$$

For the denominator we write

$$\beta - \alpha = \frac{1}{2}\ln\left[\frac{(B-b+A)(B-A)}{(B-b-A)(B+A)}\right] = \frac{1}{2}\ln\left[\frac{B^2 - A^2 - bB + bA}{B^2 - A^2 - bB - bA}\right].$$

Now, from (11) we know that for the first two terms in this fraction

$$B^2 - A^2 = R_2{}^2$$

and for the third summand

$$bB = \frac{1}{2}(R_2{}^2 - R_1{}^2 + b^2),$$

that is (using (20))

$$\lim_{b\to 0}(bB) = \frac{1}{2}\left(R_2{}^2 - R_1{}^2\right) = \lim_{b\to 0}(bA).$$

Due to continuity of the natural logarithm, putting all this together leads to

$$\lim_{b\to 0}(\beta - \alpha) = \frac{1}{2}\lim_{b\to 0}\left(\ln\left[\frac{R_2{}^2 - bB + bA}{R_2{}^2 - bB - bA}\right]\right)$$
$$= \frac{1}{2}\ln\left(\frac{R_2{}^2}{R_1{}^2}\right) = \ln\left(\frac{R_2}{R_1}\right). \tag{21}$$

Since all limits exist, one can then safely divide (20) by (21) and we straightforwardly arrive at

$$F_e(0) = \lim_{b \to 0} F_e(b) = F_c. \tag{22}$$

Similar but more tedious calculations involving the first- and second-order derivatives of F_e show that

$$\left. \frac{\mathrm{d}F_e(\varepsilon)}{\mathrm{d}\varepsilon} \right|_{\varepsilon=0} = 0 \tag{23}$$

and finally

$$\left. \frac{\mathrm{d}^2 F_e(\varepsilon)}{\mathrm{d}\varepsilon^2} \right|_{\varepsilon=0} = \pi \Delta p (R_2 - R_1) \frac{\left(R_2{}^2 - R_1{}^2\right) - \ln\left(R_2/R_1\right)\left(R_2{}^2 + R_1{}^2\right)}{\ln^2\left(R_2/R_1\right)\left(R_2 + R_1\right)}. \tag{24}$$

Substituting (22)–(24) into Equation (19) and omitting cubic and higher order terms leads to

$$F_e \approx F_c + \frac{1}{2}\left(\pi \Delta p(R_2 - R_1) \frac{(R_2{}^2 - R_1{}^2) - \ln(R_2/R_1)(R_2{}^2 + R_1{}^2)}{\ln^2(R_2/R_1)(R_2 + R_1)}\right)\varepsilon^2. \tag{25}$$

Replacing F_c in the above expression with Equation (7), factoring out this contribution as well as another term $R_2{}^3$ in both numerator and denominator, one finally arrives at relation (1), i.e.

$$F_e \approx F_c(1 + a(\kappa)\,\varepsilon^2),$$

with

$$a(\kappa) = -(1-\kappa)\frac{(1-\kappa^2) + (1+\kappa^2)\ln\kappa}{2\left(\kappa^2 + \dfrac{(1-\kappa^2)}{2\ln\kappa}\right)(1+\kappa)\ln^2\kappa}, \quad \text{where } \kappa = \frac{R_1}{R_2}. \tag{26}$$

This is the main result of this article; a relation that approximates the eccentric shear force by its concentric counterpart and a correction term that depends on the relative eccentricity and the ratio of the radii involved.

While expression (26) is valid for all values of κ, in many practical applications R_1 is close to R_2 and therefore $\kappa \approx 1$. In this case $a(\kappa)$ is already specified sufficiently enough by its linear contribution and evaluating the relevant derivative then leads to relation (2), i.e.

$$F_e \approx F_c\left(1 + \frac{(\kappa - 1)}{6}\varepsilon^2\right) \quad \text{for } \kappa \approx 1.$$
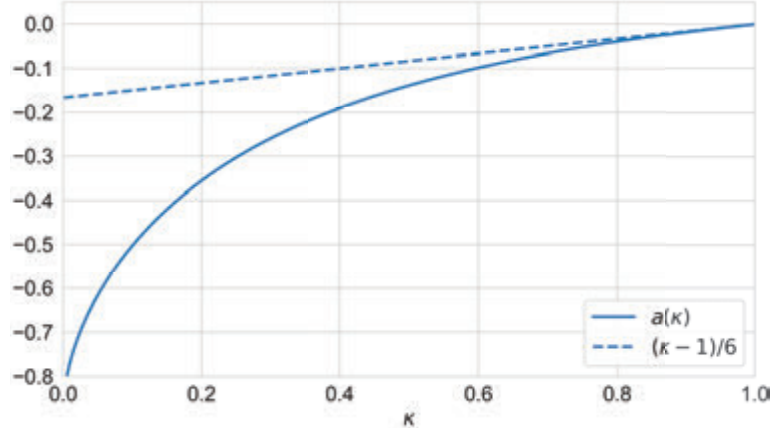
Figure 7   Variation of the correction term $a(\kappa)$ and its linear approximation at $\kappa = 1$ when increasing the ratio of inner to outer radius.

This approximation mimics the well-known Piercy-relation for the flow rate and extends it in a similar fashion to jet forces as well.

In order to work out the similarities and differences between the different approaches, we define

$$Q_c^\varepsilon := Q_c(1 + 1.5\,\varepsilon^2) \tag{27}$$

and

$$F_c^\varepsilon := F_c(1 + a(\kappa)\,\varepsilon^2). \tag{28}$$

Both definitions can be understood as expressions mainly dominated by the concentric part but modified by a smaller contribution that depends on eccentricity. This will avoid confusion when we want to compare (15) with its approximation (27) and (10) with (28) respectively.

It's immediately obvious that the constant coefficient of the quadratic correction term in Equation (27) does trivially not include any information about the actual geometry (e.g. the radius of bushing and/or housing in Figure 6). In contrast, the corresponding factor in (28) depends in a rather intricate way on κ, i.e. the ratio of inner to outer radius; see (26). It is also depicted in the following Figure 7.

In addition, the linear approximation of a at $\kappa = 1$ is shown there as well. As one can see there is a reasonable agreement between these two graphs for $\kappa \geq 0.6$.

It is worth pointing out, that [21] were well aware of the fact, that their prefactor is not constant at all, but also depends on the ratio of the
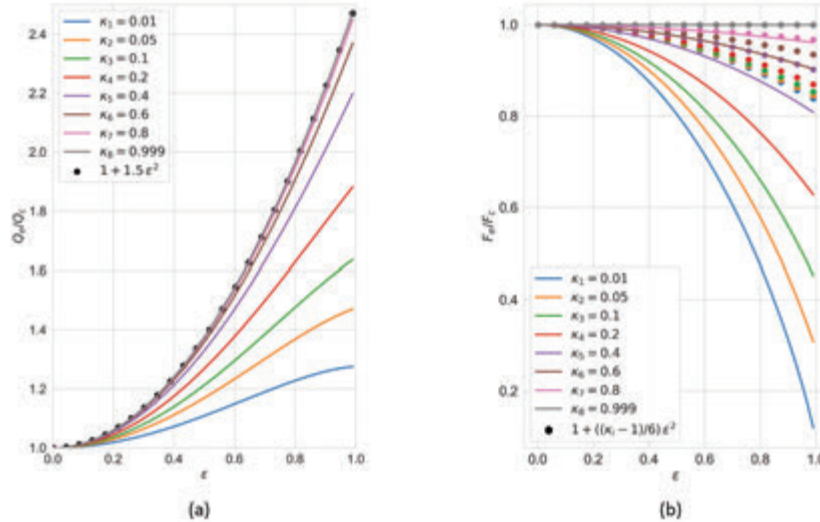
Figure 8   (a) Ratio of eccentric to concentric flow rates and (b) corresponding jet forces (solid), as well as their proposed approximations which are valid for $\kappa \geq 0.6$ (dotted).

radii involved. This is depicted in the following Figure 8(a) which compares Q_e/Q_c obtained from (15) on the one hand (solid) with corresponding values computed from (27) on the other hand (dotted); in both cases Q_c is evaluated using (13). This figure already appeared in the aforementioned paper and clearly shows that the Piercy-relation (27) is valid only for $\kappa \geq 0.6$.

Figure 8(b) shows a similar comparison for the jet forces, i.e. (10) vs. (2); F_c is obtained from (7). One can clearly see that the simple relation (2) is a very good approximation as long as $\kappa \geq 0.6$ and can therefore be regarded as equivalent to the Piercy-relation for the flow rate.

However, in addition to Equation (2) we also derived the entire corresponding 2nd-order approximation (in relative eccentricity ε); see relation (28). It should adequately describe the behaviour of the jet forces for an even wider range of possible κ. This is indeed the case as can be seen in the following Figure 9.

In contrast to the previous case it is obvious that Equation (28) proposed in this paper is a suitable approximation for all values of κ. Only when considering large eccentricities and huge differences between inner and outer radius, higher-order corrections to (28) become relevant. But as already mentioned before, in the same regime where the Piercy-relation holds, (28) could easily be replaced by its much simpler version (2).
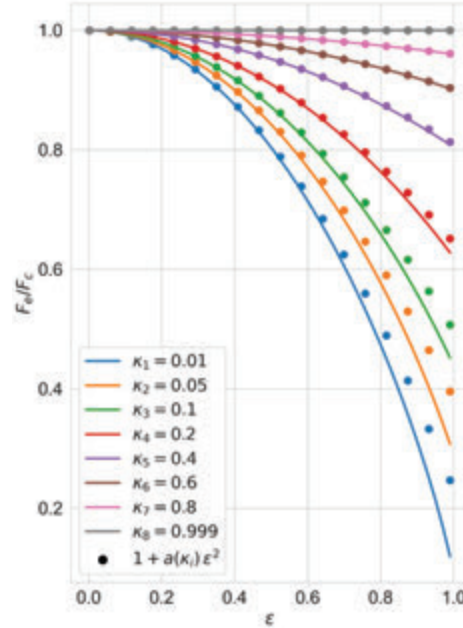
Figure 9   Comparison of relative jet forces, exact (solid) vs. full 2nd-order approximation (dotted).

In order to further check the accuracy of both F_e and its suggested alternative F_c^ε, the following Section 4 will compare them with results obtained from 3D CFD-simulations.

4 Numerical Modelling and Comparison of Leakage Jet Forces

In order to evaluate whether the assumption of a purely axial flow is in fact justified in the cases studied here, a 3D-simulation is performed in the leakage flow domain between bushing and spool as depicted in Figure 6.

The initial overlap in our example valve was 0.6 mm, however different designs might also lead to different overlaps so as a second test case, a value of 1.55 mm was chosen as well. The task is then to solve the laminar and incompressible, steady-state Navier-Stokes system (4),(5) for prescribed geometries and boundary conditions.

Ansys CFX was used to carry out FVM-simulations for the general setup described in Section 1 and depicted in Figures 1, 2. The following
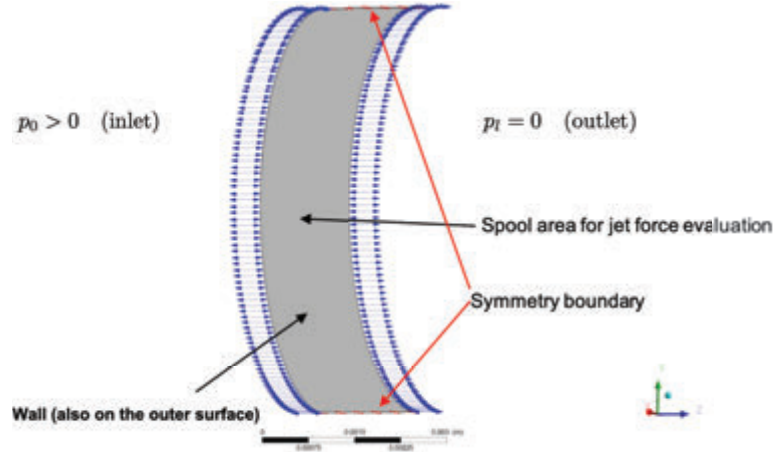
Figure 10   Half symmetric computational domain and corresponding boundary conditions for 1.55 mm overlap; only the inner cylinder surface is visible.

**Table 1**   Summary of parameters for numerical leakage simulation

Data	Value	Unit
$\Delta p = p_0 - p_l$	10 & 40	bar
R_1	3.29	mm
R_2	3.3	mm
κ	0.997	–
μ	10.11	mPa s
ρ	805	kg/m^3
b	$\varepsilon(R_2 - R_1)$	mm
l	0.6 & 1.55	mm
no. of nodes (overlap 0.6 mm)	1,012,112	–
no. of elements (overlap 0.6 mm)	932,400	–
no. of nodes (overlap 1.55 mm)	2,588,352	–
no. of elements (overlap 1.55 mm)	2,408,700	–

Figure 10 illustrates in more detail the computational domain and the boundary conditions chosen here.

Some relevant information about the geometrical and numerical specifications for the simulations is summarized in Table 1.

Figure 11   Mesh for the expected laminar fluid flow, dominated by the axial component.
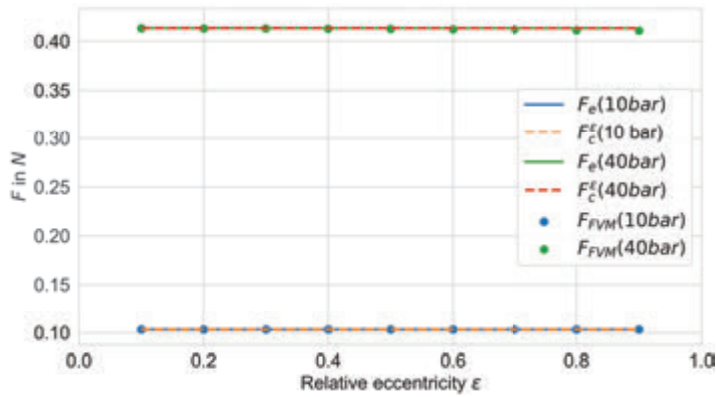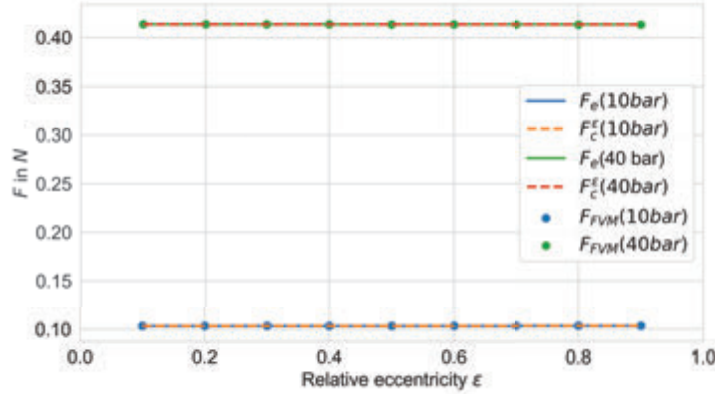

Figure 12   Comparison of numerically and analytically obtained jet forces for 10 bar and 40 bar pressure drops and an overlap of 0.6 mm.

Particular care has to be taken of an appropriate meshing of the computational domain. For cases in which the flow is dominated mainly by the axial velocity component and varies smoothly with distance from the symmetry axis, a sweep meshing method with radial boundary refinement is used; see the following Figure 11 as an example.

In order to compare the analytical expression for F_e, i.e. relation (10), and its proposed approximation F_c^ε (which by contrast trivially includes the concentric case, see Equation (28)) to numerical results, the jet force F_{FVM} obtained from the 3D-simulations is evaluated for eccentricities $\varepsilon = 0.1, 0.2, \ldots, 0.9$.

In the following Figure 12 one can see, how well our relation for the jet force performs when benchmarked against both numerically obtained forces and the original analytical relation for F_e.

For the comparison shown in Figure 12, an overlap of 0.6 mm was used. However, results are identical for the second test case considered here, i.e.

Figure 13   Comparison of numerically and analytically obtained jet forces for 10 bar and 40 bar pressure drops and an overlap of 1.55 mm.

an overlap of 1.55 mm; see the following Figure 13. As expected from the analytic expressions, there is no noticeable influence of the overlap on the jet forces; they are virtually identical for both values considered here.

The relative difference between the proposed relation (28) and the numerical results is less than 0.6 % which emphasizes the good accuracy of our approximation for F_e. The reason for this agreement is partly because the requirements for its application are met in this case, i.e. a clearly laminar behaviour of the fluid flow as highlighted in the following Figure 14 (see also Figure 10).

Even though it is not apparent from Figures 12, 13, the quality of the approximation proposed in this article depends on the correctness of its underlying assumptions, one of them being that the resulting flow can be described by the linear Stokes equation, therefore neglecting turbulence. The following Table 2 summarizes Reynolds number (*Re*) and maximum values of the velocity components (v_x, v_y, v_z) in the Cartesian system used for the simulation. Keep in mind, that $v_z = u$ in the nomenclature developed in Sections 2 and 3.

It's obvious from the data presented in Table 2, that the simulation with a pressure difference of 10 bar and an overlap of 1.55 mm leads to the smallest Reynolds number as well as the largest ratio of axial to radial velocity components, that is $v_z/(v_x^2 + v_y^2)^{1/2} \geq 23$. This would signal both a laminar and an axially dominated flow, i.e. the two assumptions that are prerequisites for applying the proposed relation (28). On the other hand, based on the same reasoning one would expect the largest deviation from our approximation in
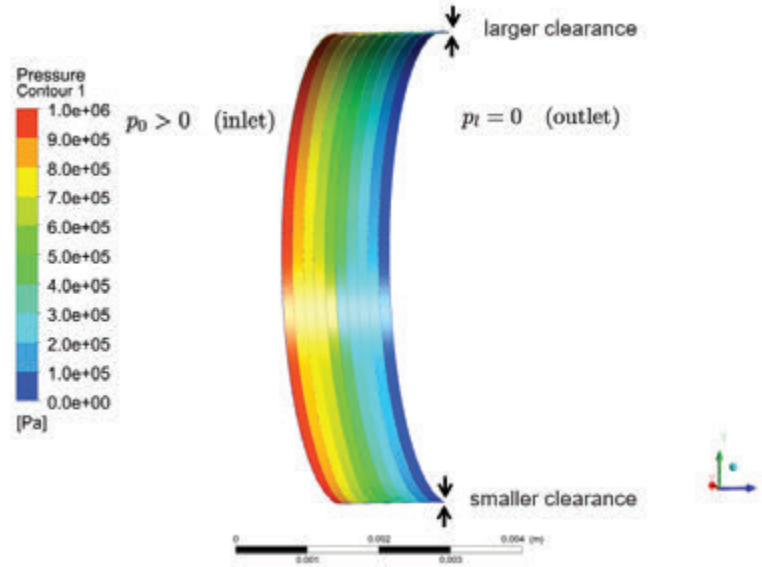
Figure 14   Linear pressure distribution for an overlap of 1.55 mm, relative eccentricity of 0.8 and a 10 bar pressure-drop.

Table 2   Reynolds number and component-wise speed maxima obtained from the CFD-simulations, velocities are given in $\mathrm{m\,s^{-1}}$.

|	10 bar, 0.6 mm	10 bar, 1.55 mm	40 bar, 0.6 mm	40 bar, 1.55 mm
Re	66.61	35.53	262.02	141.77
$(v_x)_{\max}$	0.18	0.04	0.96	0.32
$(v_y)_{\max}$	0.40	0.1	1.91	0.71
$(v_z)_{\max}$	6.59	2.55	25.7	10.3

the corresponding simulation of a 40 bar-pressure drop and an overlap of 0.6 mm.

These predictions are corroborated by the following Figures 15 and 16, which are zoomed-in versions of the relevant curves already depicted in Figures 12, 13.

Although the differences are minuscule from a practical point of view, the figures still show vividly how good relation (28) approximates the analytical solution (10) of the linear Stokes equation and how both approaches, strictly speaking, fail once the corresponding fluid flow gets more turbulent and less axially dominated.
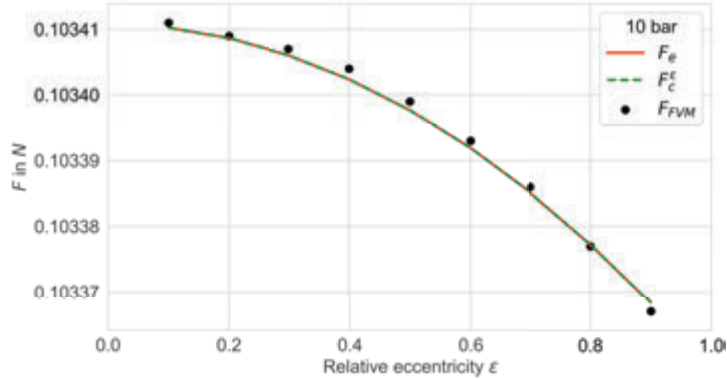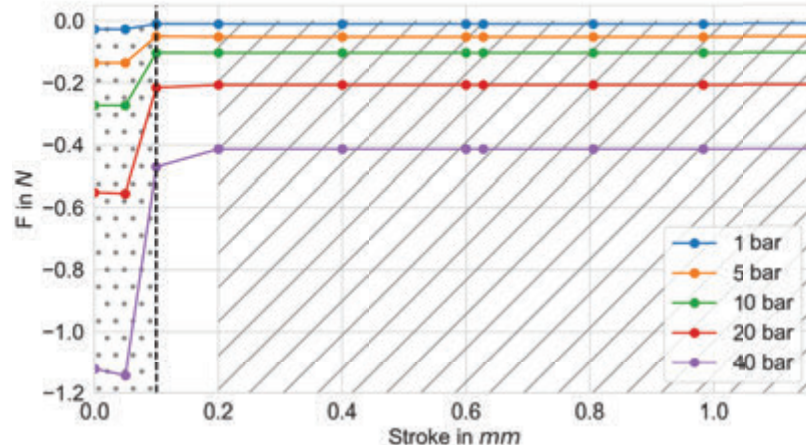
Figure 15   Comparison of numerical and analytical forces for a 10 bar pressure drop and an overlap of 1.55 mm (scaled-up from Figure 13).
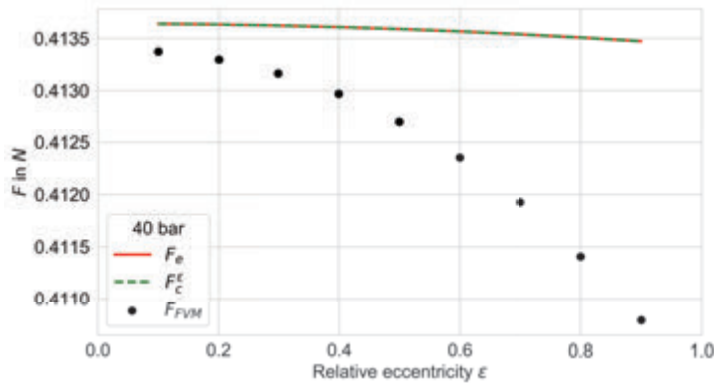
Figure 16   Comparison of numerical and analytical forces for a 40 bar pressure drop and an overlap of 0.6 mm (scaled-up from Figure 12).

On the other hand, especially Figures 12 and 13 show that apart from this rather academic discussion, even stronger violations of the assumptions required for applying (28) still lead to a good estimate of the jet forces for all practical purposes. A rigorous study of the sensitivity of the proposed approximation with respect to the ratio δ/l (annular gap divided by overlap) with methods from asymptotic analysis (as used in [19]) could be the content of future work.

The following Figure 17 finally answers the question of how the jet forces can be modelled when the path BT is closed. For geometries like concentric or eccentric gaps, analytical approximations like relation (28) are applicable.

Figure 17   Completion of numerically obtained shear forces by analytically computed shear forces; compare with Figure 5.

The last Section 5 will describe an experimental setup to gauge the accuracy of the combined numerical/analytical model of the jet forces for usage in a digital twin.

5 Experimental Testing and Validation of the Combined Model

In order to illustrate the accuracy of the response from the digital twin schematically depicted in Figure 4, numerical and analytical input fields were generated by post-processing 3D-simulations as well as utilizing relations like (27) and (28). The digital twin described in Section 2 is then included in an Amesim model of the hardware test rig. The oil temperature (determined by the ambient temperature of the climate chamber), which dictates the relevant CFD-fields for the system simulation model, can be set via the Amesim component "FP04"; see also [7] or [11] for further details on using input data with Amesim. Finally, the numerically obtained flow rates are compared to corresponding measurements from the test rig, including the hardware twin of the valve.

The following Figure 18 depicts the Hilite test rig used for hydraulic measurements of a flow regulating valve. Since the test bench is employed for other measurements as well, the overall setup shown here is slightly larger than required.
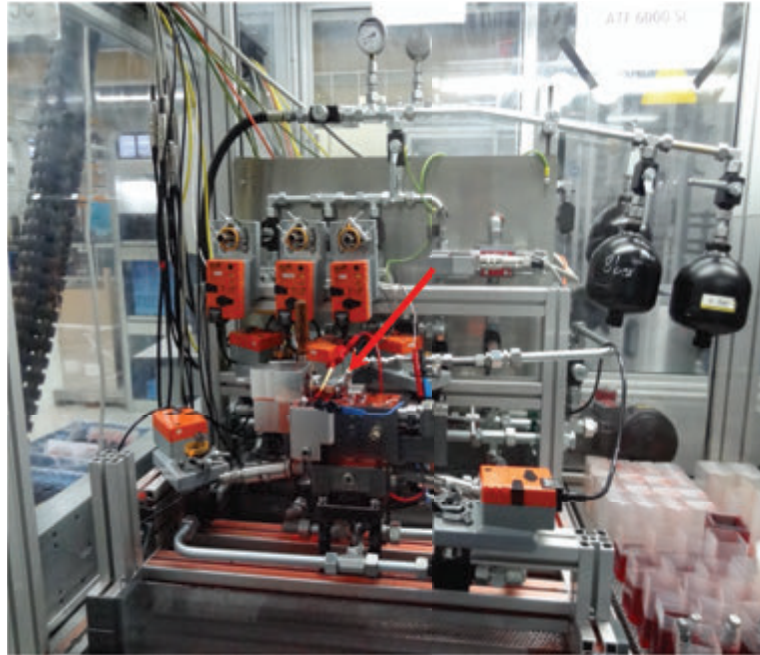
Figure 18   Test rig used for measuring flow rates; the red arrow points to the actual valve within this setup.
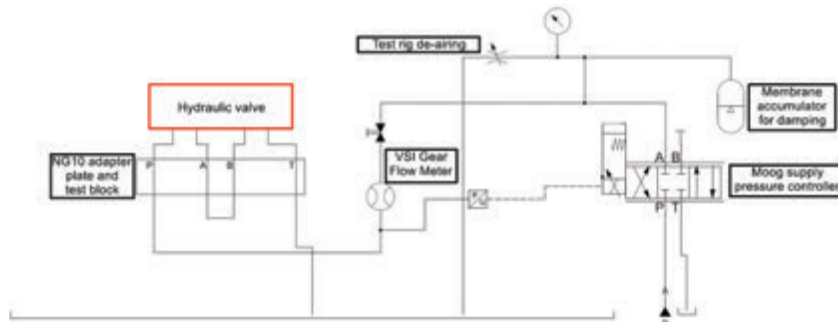
Figure 19   Reduced hydraulic scheme; the valve to be measured is outlined in red.

The reduced hydraulic scheme corresponding to this setup is depicted in Figure 19; the actual valve that is marked by an arrow in previous Figure 18 is outlined in red here.

A direct acting servo valve by Moog is used for adjusting the supply pressure. It features a very short response time and is used in our test benches
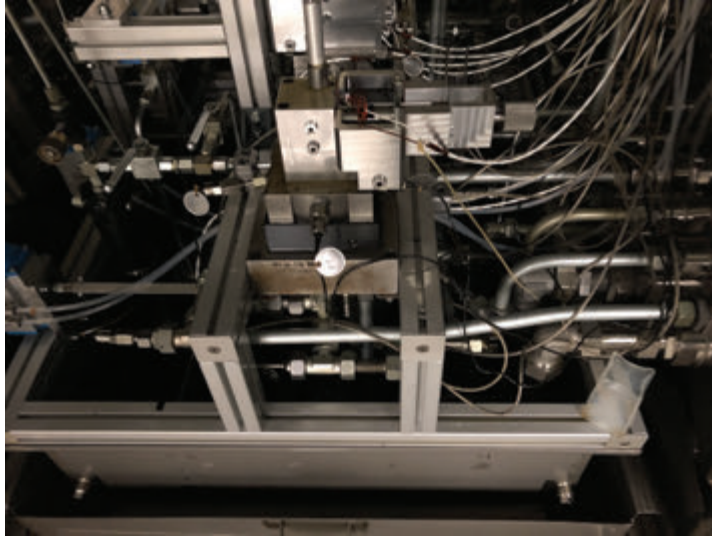
Figure 20   Interior view of the CTS temperature test chamber.

for facilitating static supply pressures and to eliminate pressure differences during each single test. The built-in accumulator prevents undesired pressure oscillations. Prior to the inlet a VSI gear flow meter is employed for measuring the flow rate. In this type of device gear rotation is monitored by a non-contacting signal pickup system. This allows for a precise determination of the fluid volume that is enclosed in the measuring chambers between the gear teeth. The VSI is a pre-amplifier that greatly improves signal quality, leading to measurement errors below 0.3% within a temperature range from $-40°$ C to 120°C.

A Kulite pressure sensor placed between gear flow meter and valve is used in a feedback-loop with the Moog controller to monitor and adjust the pressure on the inlet of the valve. The sensor is calibrated for all specified temperatures before starting any flow measurements in order to achieve a high accuracy.

For measurements at different temperatures the entire test rig can be put into a CTS conditioning chamber; see the following Figure 20.

In this way, it is possible to simulate and adjust for environmental influences on the valve as well as attached transmission components. This is a standard test procedure for automotive testing and it allows for separate heating/cooling of fluid and environment. The CTS chamber is set to the required temperature and in addition, the fluid (oil in this case) is also cooled
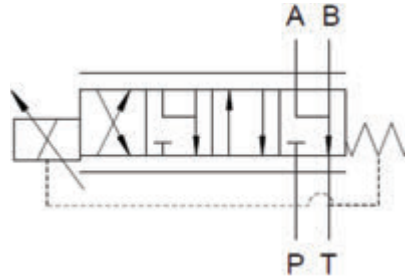
Figure 21   Fluid circuit diagram of the valve used for testing.

or heated. When the chamber has reached the necessary temperature there is an auxiliary holding time of about 6 hours so that chamber, fluid and test rig can achieve thermal equilibrium.

A schematic diagram of the measured valve is depicted in the following Figure 21.

In this case, it is a 4/4 proportional valve with an adjustable solenoid acting from the left (as indicated by the corresponding symbol, see also Figure 3). In its neutral position, a floating condition is achieved while blocking the connection to the pump and no fluid flow will occur. Once energized, the solenoid will move the spool inside the bushing so that with increasing stroke fluid is passing from pressure inlet P (a supply pressure of 10 bar is applied here) to port A and from port B back to the reservoir T respectively. Moving further, another floating position with zero volume flow is reached before the high pressure inlet P is connected to B and accordingly port A back to the reservoir T.

For measurements the solenoid contained within the valve is subjected to a current ramp. After a brief currentless activation at the start of this routine (automated postprocessing of data is initiated here), the electric current is increased with a ramp speed of 33 mA/s before reaching its final value of 1000 mA after roughly 30 seconds. From this maximum the current is decreased to 0 A at the same speed. In addition to this current ramp there is also a harmonic dither-signal with a frequency of 125 Hz and an amplitude of 250 mA which is superimposed to the carrier current.

The following Figure 22 depicts the time-dependent current variation outlined above.

All signals are recorded with an initial sampling frequency of 30 kHz and are then subsequently downsampled to 10 kHz in order to reduce the amount of data to be processed. As required by most of the customers, the signals are
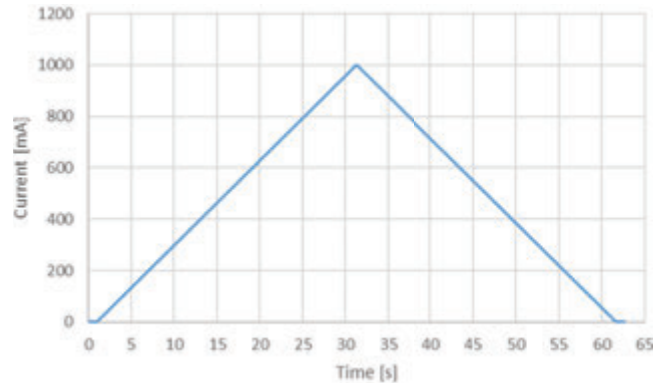
Figure 22   The variation of electric current with time used for the flow rate measurements; dither-signal not included here.
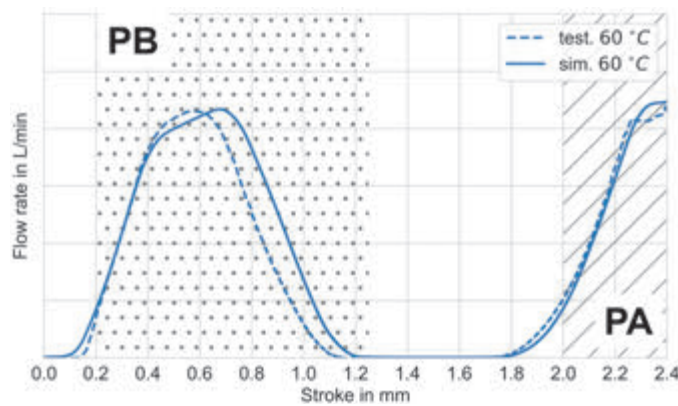

Figure 23   Comparison between simulated and measured flow rate (average of rising and falling segments) at a temperature of $60°$ C.

filtered afterwards with a 4th-order Bessel filter employing a cutoff-frequency of 10 Hz and separated into rising and falling segments according to the current ramp of Figure 22.

The following Figure 23 shows the characteristic flow curve obtained as an average over rising and falling segments for the digital twin and compares it to the corresponding measurements at an operating temperature of $60°$ C. Due to required confidentiality, the y-axis needs to remain unlabelled.

As one can see, the agreement between simulation and measurement is very good. The areas in which PA and PB are open are marked with point and line patches respectively. The flow outside of the marked areas is due
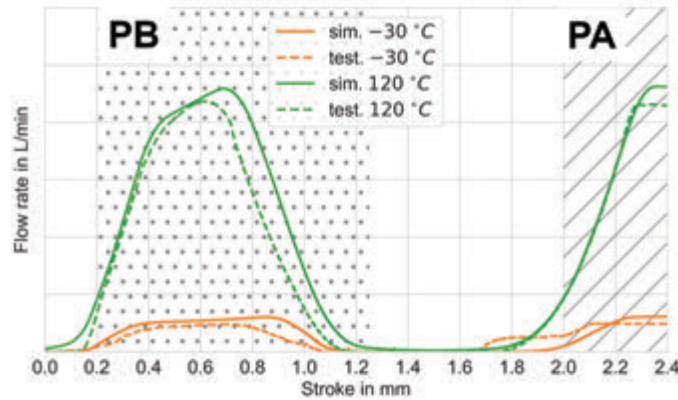
Figure 24   Same as Figure 23 but for $-30°$ C and $120°$ C.

to partial openings due to the spool geometry (see Figure 3), the connection of PB and AT and PA and BT respectively and internal leakage. This also extends to other temperatures as well; see the following Figure 24.

As expected, mainly due to viscous effects which increase for lower temperatures, the flow rates decrease significantly when dropping the temperature; see also Equations (13), (15). While there are slightly larger deviations between simulation and measurement, the overall agreement is still satisfactory.

This comparison shows the usefulness of employing proper modelled digital twins of valves in system simulations in order to optimize the performance of these elements as components of larger transmission assemblies.

6 Conclusion

In this work an analytical approximation for the shear force, which is induced by viscous flow between two cylinders, is presented. This relation, as well as its derivation, mimics the well-known Piercy-approach for the corresponding volume flow which involves the relative eccentricity as an expansion parameter for a Taylor-series. While the latter one is strictly valid only in a certain limiting case (that is nevertheless mostly fulfilled in practical applications), the approximation for the shear forces proposed here exhibits a much broader range of validity. Its utilization is restricted only by the inherent limitation of a truncated series expansion and the requirement of a laminar, axially dominated fluid flow.

These findings were corroborated by comparisons with 3D-simulations of the complete Navier-Stokes equations. The detailed case studies not only showed under which circumstances our approximation will fail to hold but also how minute the observed discrepancies between analytical and numerical results are. From this point of view, our statement about the suggested domain of validity is rather a mathematical conclusion than something that would severly limit the application of our relation for the jet forces in any realistic scenario. In fact, it could be implemented quite universally for example in subsequent releases of the Simcenter Amesim component "BRF01". This would also neatly fit with other components, e.g. "HYDORG11", that already utilize similar analytical estimates.

As an application example, the proposed approximation for jet forces was applied for the generation of input fields for a digital twin. These are needed by system simulation software in order to accurately predict the behaviour of actual, real devices on which the corresponding digital counterparts are based upon. Proper modelled components also help to optimize preliminary designs in a cost-effective manner. Of course, the success of this approach stands and falls by the accuracy of the digital reproduction of a physical object. The procedure presented here in case of a magneto-hydraulic valve leads to a very good agreement between simulation and measurements. This will undoubtedly encourage and foster the development of hydraulic systems by exchanging digital twins between vendors and customers in a modern, networked environment.

7 Nomenclature

R_1	radius of inner cylinder
R_2	radius of outer cylinder
δ	annular gap/clearance between cylinders, i.e. $R_2 - R_1$
κ	ratio of inner and outer cylinder radius, i.e. R_1/R_2
b	absolute eccentricity/shift of inner cylinder
ε	relative eccentricity/shift of inner cylinder, i.e. b/δ
p_0	pressure at inlet
p_l	pressure at outlet
Δp	pressure drop, i.e. $p_0 - p_l$
F_e	flow force in the eccentric case
F_c	flow force in the concentric case
Q_e	flow rate in the eccentric case

Q_c flow rate in the concentric case

Q_c^ε known approximation of eccentric flow rate, as correction of Q_c

F_c^ε new approximation of eccentric jet force, a truncated expansion of F_e

Q_1 leading term of Taylor-expansion of Q_c in δ, around $\delta = 0$

Q_2 first two non zero terms of mentioned Taylor-expansion of Q_c

Q_3 first three terms of mentioned Taylor-expansion of Q_c, not seen by authors in literature

μ dynamic viscosity of fluid

ρ density of fluid

v   fluid velocity field, whith radial components v_x, v_y and axial contribution $v_z = u$

p pressure of fluid

References

[1] Yutaka Abe, Hajime Akimoto, and Yoshio Murao. Estimation of shear stress in counter-current annular flow. *Journal of Nuclear Science and Technology*, 28, 1991.

[2] Riccardo Amirante, Elia Distaso, and Paolo Tamburrano. Sliding spool design for reducing the actuation forces in direct operated proportional directional valves: Experimental validation. *Energy Conversion and Management*, 119, 2016.

[3] Riccardo Amirante, G. Vescovo, and Antonio Lippolis. Flow forces analysis of an open center hydraulic directional control valve sliding spool. *Energy Conversion and Management*, 47, 01 2006.

[4] R.B. Bird, E.N. Lightfoot, and W.E. Stewart. *Transport Phenomena*. J. Wiley, 2002.

[5] Patrik Bordovsky, Katharina Schmitz, and Hubertus Murrenhoff. Cfd simulation and measurement of flow forces acting on a spool valve. In *10th International Fluid Power Conference , Dresden , Germany*, 2016.

[6] Wilson C. Chin. Chapter 4 - steady, two-dimensional, non-newtonian, single-phase, eccentric annular flow. In Wilson C. Chin, editor, *Managed Pressure Drilling*. Gulf Professional Publishing, 2012.

[7] Christian Hugel. Optimization of a piston geometry in a pressure control valve. RDO Journal Issue 2, 2016.

[8] Christian Hugel. Optimization of an actuators magnetic force with optislang. RDO Journal Issue 2, 2019.

[9] D. Joseph, Ruijing Bai, Kang Chen, and Yuriko Renardy. Core-annular flows. *Annu. Rev. Fluid Mech.*, 29, 11 2003.

[10] E.M. Khaĭmovich. *Hydraulic Control of Machine Tools*. Pergamon Press, 1965.

[11] Johannes Krebs. optislang in functional development of hydraulic valves. RDO Journal Issue 2, 2019.

[12] Francois Laborie, Ole Christian Røed, Geir Engdahl, and Audrey Camp. Extracting value from data using an industrial data platform to provide a foundational digital twin. Offshore Technology Conference, 2019.

[13] L.D. Landau and E.M. Lifshitz. *Fluid Mechanics: Volume 6*. Elsevier Science, 2013.

[14] Ryan Magargle, Lee Johnson, Padmesh Mandloi, Peyman Davoud-abadi, Omkar Kesarkar, Sivasubramani Krishnaswamy, John Batteh, and Anand Pitchaikani. A simulation-based digital twin for model-driven health monitoring and predictive maintenance of an automotive braking system. 2017.

[15] Noah Manring. Modeling spool-valve flow forces. ASME 2004 International Mechanical Engineering Congress and Exposition, 2004.

[16] Mario Neto and Luiz Goes. Use of lms amesim model to predict behavior impacts of typical failures in an aircraft hydraulic brake system. In *Proceedings of 15th Scandinavian International Conference on Fluid Power*, pages 29–43, 12 2017.

[17] Jarmo Nurmi and Jouni Mattila. Detection and isolation of leakage and valve faults in hydraulic systems in varying loading conditions, part 1: Global sensitivity analysis. *International Journal of Fluid Power*, 2011.

[18] Michael Païdoussis. *Annular- and Leakage-Flow-Induced Instabilities*. 12 2016.

[19] Grigory Panasenko and Konstantin Pileckas. Asymptotic analysis of the nonsteady viscous flow with a given flow rate in a thin pipe. *Applicable Analysis*, 91, 2012.

[20] Enrico G. Pasquini. *Eindimensionale Berechnung instationärer Ringspaltströmungen mit thermofluiddynamischer Betrachtung*. Reihe Fluidtechnik, RWTH Aachen, 2020.

[21] N.A.V. Piercy, M.S. Hooper, and H.F. Winny. Liii. viscous flow through pipes with cores. *The London, Edinburgh, and Dublin Philosophical Magazine and Journal of Science*, 1933.

[22] R.K. Shah and A.L. London. Laminar flow forced convection in ducts. Academic Press, 1978.

[23] Marko Šimic, Mihael Debevec, and Niko Herakovič. Modelling of hydraulic spool-valves with special designed metering edges. *Strojniški vestnik-Journal of Mechanical Engineering*, 60(2):77–83, 2014.

[24] Jeffrey Tithof, Douglas H Kelley, Humberto Mestre, Maiken Neder-gaard, and John H Thomas. Hydraulic resistance of periarterial spaces in the brain. *Fluids and Barriers of the CNS*, 16, 2019.

[25] Frank M White. *Fluid mechanics*. Tata McGraw-Hill Education, 1979.

[26] Frank M. White. *Viscous fluid flow*. McGraw-Hill New York, 2006.

[27] Holger Zipper, Felix Auris, Anton Strahilov, and Manuel Paul. Keeping the digital twin up-to-date — process monitoring to identify changes in a plant. *2018 IEEE International Conference on Industrial Technology (ICIT)*, 2018.

Biographies

Zoufiné Lauer-Baré currently works as simulation engineer in the development of electro-hydraulic valves. He received his Ph.D. in 2014 at the Fraunhofer Institute for Industrial Mathematics (ITWM) and the TU Kaiserslautern. The topic of his thesis was the modeling of elastic rod structures.

Erich Gaertig finished his Ph.D. in theoretical astrophysics at the University of Tübingen in 2008. After further postdoc studies and a short interlude as

development engineer, working on novel numerical approaches, he joined the simulation group at Hilite. There, he is mainly responsible for electromagnetic field calculation of actuators. Other areas of interest include modelling and numerical/analytical methods in physics and engineering.

Johannes Krebs currently works as a simulation manager at the simulation department. He is responsible for the transmission simulation. After he finished his thesis in numerical fluid- and aerodynamics at the University of Stuttgart (IAG) in 2014, he started at Hilite as a CFD-simulation specialist. Other fields he is working on are system simulation and the modelling of digital valve systems including DOE and robust design analysis.

Christian Arndt finished his study of Aerospace Engineering at the University of Stuttgart in 2008. After that he worked as simulation engineer in the development of gasoline engines with focus on 1D- and 3D-CFD simulations. He joined Hilite in 2016 where his field of work are system simulations as well as 3D-CFD simulations in the development of hydraulic cam phaser systems.

Christian Sleziona received his Ph.D. in Plasma Propulsion at the University of Stuttgart. He finished his postdoctoral thesis on Hypersonic Flows and started as professor for Hypersonic Aerothermodynamics at Tohoku University in Japan. After working at the ITWM of the University of Kaiserslautern and IHI Charging Systems International, he currently works as head of the simulation department at Hilite.

André Gensel currently works as a manager at testing department. He is responsible for transmission valve testing. He joined Hilite in 2014 after he finished his diploma thesis in reducing of drag torque on wet running multiplate clutch systems at Brandenburg University of Technology (BTU).